

# The 2019–2020 Khalili (Iran) earthquake sequence — anthropogenic seismicity in the Zagros Simply Folded Belt?

Mohammadreza Jamalreyhani<sup>1,2</sup>, Léa Pousse-Beltran<sup>3,4</sup>, Pınar Büyükakpınar<sup>5</sup>, Simone Cesca<sup>2</sup>, Edwin Nissen<sup>3</sup>, Abdolreza Ghods<sup>6</sup>, José Ángel López-Comino<sup>7,8,9</sup>, Mehdi Rezapour<sup>1</sup>, Mahdi Najafi<sup>6</sup>

<sup>1</sup>Institute of Geophysics, University of Tehran, Iran.

<sup>2</sup>GFZ German research center for Geosciences, Potsdam, Germany.

<sup>3</sup>School of Earth and Ocean Sciences, University of Victoria, Victoria, British Columbia, Canada

<sup>4</sup>Univ. Grenoble Alpes, Univ. Savoie Mont Blanc, CNRS, IRD, UGE, ISTerre, 38000 Grenoble, France

<sup>5</sup>Kandilli Observatory and Earthquake Research Institute, Boğaziçi University, İstanbul, Turkey.

<sup>6</sup>Department of Earth Sciences, Institute for Advanced Studies in Basic Sciences, Zanjan, Iran.

<sup>7</sup>Instituto Andaluz de Geofísica, Universidad de Granada, Granada, Spain.

<sup>8</sup>Departamento de Física Teórica y del Cosmos, Universidad de Granada, Granada, Spain.

<sup>9</sup>Institute of Geosciences, University of Potsdam, Potsdam-Golm, Germany.

Corresponding author: Mohammadreza Jamalreyhani ([m.jamalreyhani@gmail.com](mailto:m.jamalreyhani@gmail.com))

## Key Points:

- Discrimination of anthropogenic earthquakes in areas of naturally-elevated seismicity is challenging.
- The 2019-2020 Khalili earthquake sequence is the first well-resolved example of induced seismicity linked to gas extraction in the Zagros.
- Understanding anthropogenic and natural seismicity is important in Iran which is both seismically-active and rich in hydrocarbon reserves.

**33 Abstract**

34

35 We investigate the origin of a long-lived earthquake cluster in the Fars arc of the Zagros Simply  
36 Folded Belt that is co-located with the major Shanul natural gas field near the small settlement of  
37 Khalili. The cluster emerged in January 2019 and initially comprised small events of  $M_n \sim 3\text{--}4$ . It  
38 culminated on June 9, 2020 with a pair of  $M_w$  5.4 and 5.7 earthquakes, which were followed by  
39  $> 100$  aftershocks. We assess the spatio-temporal evolution of the earthquake sequence using  
40 multiple event hypocenter relocations, waveform inversions, and Sentinel-1 Interferometric  
41 Synthetic Aperture Radar (InSAR) measurements and models. We find that the early part of the  
42 sequence is spatially distinct from the June 9, 2020 earthquakes and their aftershocks. Moment  
43 tensors, centroid depths, and source parameter uncertainties of fifteen of the largest ( $M_n \geq 4.0$ )  
44 events show that the sequence is dominated by reverse faulting at shallow depths (mostly  $\leq 4$   
45 km) within the sedimentary cover. InSAR modelling shows that the  $M_w$  5.7 mainshock occurred  
46 at depths of 2–8 km, with a rupture length and maximum slip of  $\sim 20$  km and  $\sim 0.5$  m,  
47 respectively. Our results strongly suggest that the 2019-2020 Khalili earthquake sequence was  
48 influenced by the operation of the Shanul field, making these the first known examples of gas  
49 extraction anthropogenic earthquakes in Zagros. Understanding the genesis of such events to  
50 distinguish man-made seismicity from natural earthquakes is helpful for hazard and risk  
51 assessment, notably in Iran which is both seismically-active and rich in oil and gas reserves.

**52 Plain Language Summary**

53

54 Earthquakes caused by human activities have been documented in a growing number of regions  
55 worldwide, but recognizing these events in areas of naturally-elevated seismicity remains  
56 challenging. We investigate the origin of earthquake cluster in the Zagros mountains — one of

57 the world's most seismically active mountain belts — that is co-located with a major natural gas  
58 field. The seismicity led to public concern and speculation that nearby natural gas extraction was  
59 responsible. We assess the spatio-temporal evolution of the earthquake sequence and use satellite  
60 geodesy and seismology measurements and models. Our results support these being the first,  
61 well-resolved examples of anthropogenic earthquakes related to gas extraction in the Zagros. We  
62 suggest that the exploitation of the reservoirs in Iran should be preceded by risk assessment  
63 studies and accompanied by the implementation of dedicated, sophisticated monitoring, which  
64 would allow seismicity to be detected early and tracked more closely.

## 65 **1 Introduction**

66

67 Anthropogenic earthquakes, defined as those induced or triggered by human actions, have now  
68 been identified in many different regions across the globe (Foulger et al., 2018). Activities  
69 known or suspected to cause anthropogenic seismicity include subsurface fluid injection or  
70 extraction — through hydraulic fracturing, geothermal energy exploitation, and gas storage — as  
71 well as mining operations and water reservoir impoundment (Grigoli et al., 2017; Foulger et al.,  
72 2018; Keranen & Weingarten, 2018).

73

74 These activities can introduce pore pressure transients and alter the local stress field,  
75 consequently promoting (or inhibiting) earthquake occurrence (Ellsworth 2013, Dahm et al.,  
76 2013). Fluid injection-induced seismicity (IIS) has become particularly widespread in recent  
77 years due to increased shale gas exploitation and waste water disposal, geothermal stimulation,  
78 and gas storage (Ellsworth 2013, Foulger et al., 2018). To date, IIS has reached moderate  
79 magnitudes — for example the 2017  $M_w$  5.5 Pohang earthquake (e.g. Grigoli et al., 2018), the

80 2016  $M_w$  5.1 Fairview,  $M_w$  5.7 Prague, and  $M_w$  5.8 Pawnee, Oklahoma earthquakes (Ellsworth  
81 2013, Keranen et al., 2014, Yeck et al., 2017), and the 2013  $M_w$  4.3 earthquake in Castor gas  
82 storage (Cesca et al., 2014) — sufficient that there are often strong socioeconomic impacts  
83 (Grigoli et al., 2017).

84

85 Recognizing anthropogenic earthquakes is particularly challenging in regions of naturally-  
86 elevated seismicity, with detailed source analyses essential in order to discriminate between the  
87 two (Dahm et al., 2015). The Zagros fold-and-thrust belt within the Arabia-Eurasia collision  
88 zone (Figure 1a) offers an excellent example, comprising one of the most seismically-active  
89 mountain belts as well as one of the greatest loci of oil and gas production in the world. The  
90 outer part of the range, known as the Simply Folded Belt, is characterized by a thick (averaging  
91 ~10 km) sedimentary cover that contains hidden reverse faults that host frequent large, damaging  
92 earthquakes (e.g. Talebian & Jackson 2004; Nissen et al., 2011). The folded and faulted  
93 sediments contain 90% of Iran's proven hydrocarbon reservoirs including the world's second-  
94 largest gas reserves, estimated at ~32.0 trillion cubic meters, or ~17% of Earth's total. Having  
95 started gas production in 1990, Iran now produces more than one billion cubic meters of gas per  
96 day from 36 gas fields, most of which are located in the Fars arc in the south-eastern Zagros  
97 (Figure 1b; Esrafil-Dizaji & Rahimpour-Bonab, 2013; Vergés et al., 2011). Despite the intense  
98 hydrocarbon production, there have so far been no unequivocal cases of earthquakes linked to  
99 gas/oil extraction or waste-water disposal in the Zagros — though a few earthquakes have been  
100 attributed to reservoir impoundment (Kangi and Heidari, 2008), mining (Mansouri-Daneshvar et  
101 al., 2018) and groundwater pumping (Kundu et al., 2019).

102

103 Here, we investigate a prominent cluster of felt earthquakes near Khalili, in the central Fars arc,  
104 starting in January 2019. The swarm-like activity and its spatial association with the major  
105 Shanul gas field raised legitimate concerns of an anthropogenic cause. The sequence culminated  
106 in mid-2020 with a  $M_w$  4.7 earthquake on May 31,  $M_w$  5.4 and 5.7 earthquakes on June 9, and a  
107 sustained aftershock sequence. The largest event, at 17:18 UTC on June 9, was responsible for  
108 several injuries.

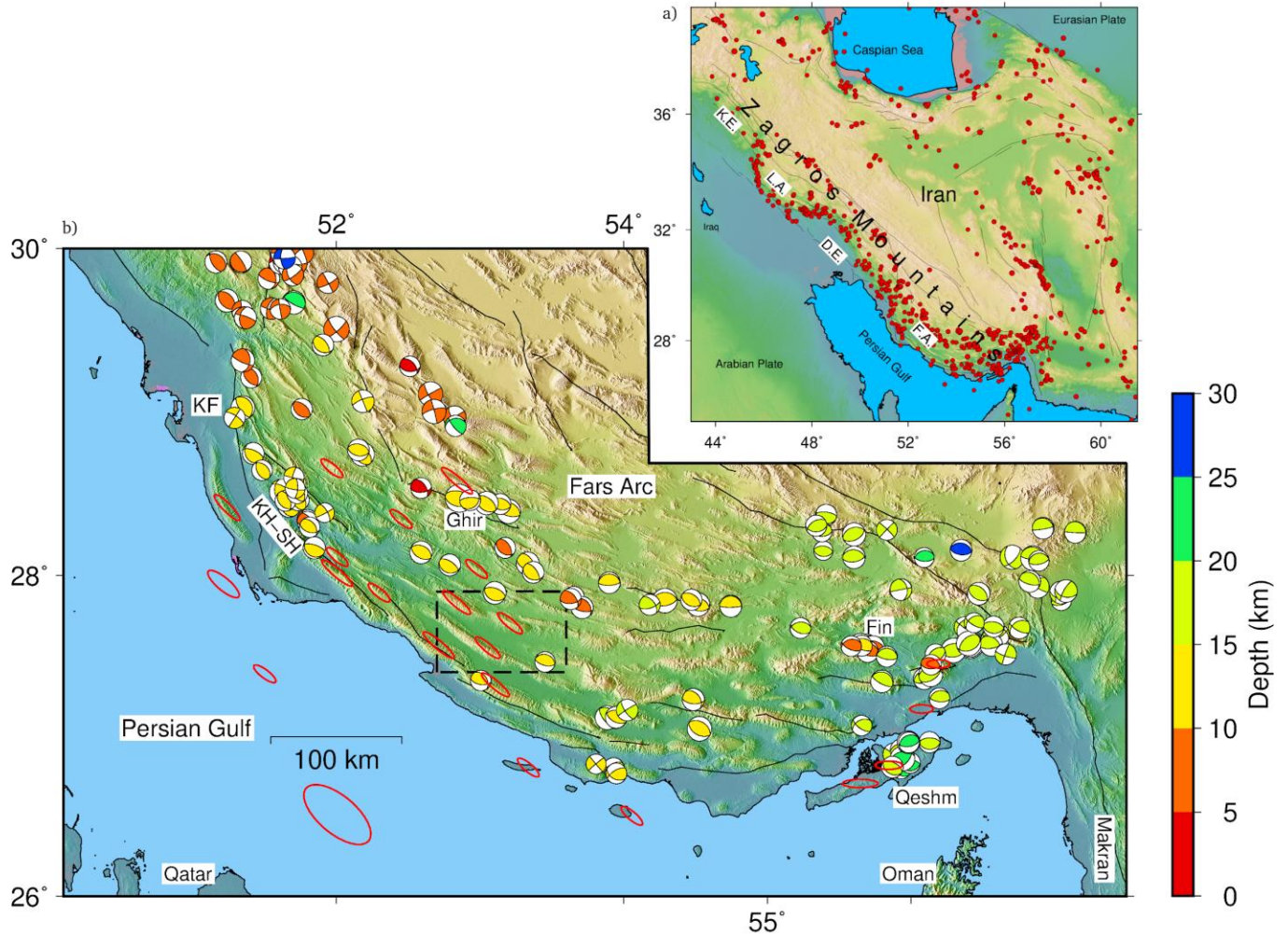
109  
110 In this study, we present a detailed analysis of the Khalili sequence to gain insights into its  
111 mechanisms and origins. By utilizing stations of the Iranian Seismological Center seismic  
112 network (IRSC; see *Data availability*), which are denser here than in many other parts of Iran,  
113 we relocated the 18 month-long sequence and calculated focal mechanisms and centroid depths  
114 for the fifteen largest ( $M_w > 4.0$ ) events. We also estimated the coseismic slip distribution of the  
115 June 9, 2020  $M_w$  5.7 mainshock using Interferometric Synthetic Aperture Radar (InSAR)  
116 measurements and elastic dislocation models. We compared the results with subsurface geology  
117 constructed using 2-D seismic profiles. Our results reveal a close spatial correlation between  
118 seismicity and extraction/injection operation in the Shanul gas field, as well as a number of  
119 anomalous source characteristics for the larger events. For the first time, we suggest a case of  
120 anthropogenic earthquakes related to gas extraction in the Zagros.

121

122

123

124



125  
 126 **Figure 1. (a)** Iranian seismicity, showing the location of the Zagros mountains at the leading edge of the Arabia-  
 127 Eurasia collision zone. Red circles are  $M > 5.0$  earthquakes from 1900–2019 from the USGS catalog. The most  
 128 active, outer part of the Zagros (simply folded belt) can be subdivided into four tectono-stratigraphic domains: from  
 129 SE to NW, the Fars arc (F.A.), Dezful embayment (D.E.), Lurestan arc (L.A.), and the Kirkuk embayment (K.E.).  
 130 **(b)** A zoom-in of the Fars arc. A large number of anticlines are evident in the topography, several of which contain  
 131 active gas fields (red ellipses). Black lines show major mapped active faults, including the right-lateral Kazerun  
 132 Fault (K.F.). Focal mechanisms from published waveform modeling studies are plotted at relocated epicenters and  
 133 coloured according to focal depth (Karasözen et al., 2019 and references therein). Notable earthquake sequences  
 134 include those at Khaki-Shonbe (KH–SH; Elliott et al., 2015), Ghir (e.g. Berberian, 1995), Fin (Roustaei et al., 2010),  
 135 and Qeshm (Nissen et al., 2010, 2014; Lohman & Barnhart, 2010). The black rectangle shows our study area (Figure  
 136 2).

137

138

## 139 **2 Background**

### 140 **2.1. Active tectonics, structure, and seismicity of the Fars arc**

141 The Fars arc refers to the arcuate part of the southeastern Zagros between the Kazerun fault in  
142 the west and the Bandar Abbas syntaxis in the east (Figure 1b). GPS measurements indicate 10  
143 mm/yr of NNE-directed convergence across the central Fars arc (e.g. Tatar et al., 2004). This  
144 shortening is manifest at the surface in symmetric, range-parallel folds with amplitudes of up to a  
145 few kilometers and wavelengths of ~10–20 km (e.g. Edey et al., 2020), and at depth in frequent  
146 earthquakes on steeply dipping (30°–60°), blind reverse faults (Berberian, 1995; Talebian &  
147 Jackson, 2004; Nissen et al., 2011). There are no known examples of coseismic surface rupture  
148 in the Fars arc, and the mechanical relationship between buried faults and surface folds remains a  
149 matter of debate.

150 The sedimentary cover of the Fars Arc is detached from the underlying basement by a layer of  
151 Ediacaran–early Cambrian Hormuz salt, which also surfaces in numerous diapirs (e.g. Jahani et  
152 al., 2009, 2017; Barnhart & Lohman 2012; Edey et al., 2020). Estimates of the depth of this  
153 interface vary from as little as ~6–8 km (e.g. Sherkati et al., 2005) to as great as ~14–20 km  
154 (Jahani et al., 2017). In the central Fars arc, closest to our study area, orogen-scale geological  
155 cross-sections interpret the basement depth to be ~8–12 km (e.g. Allen et al., 2013; Najafi et al.,  
156 2014). Analysis of local and teleseismic earthquakes collected in 1997 by a temporary (~2  
157 month) dense seismological network in the Ghir region, ~100 km north of Khalili, resolved  
158 thicknesses of 11 km and 46 km for the sedimentary cover and crust, respectively (Tatar et al.,  
159 2004).

160 InSAR and teleseismic waveform modelling studies suggest that many of the larger ( $M_w > 5$ )  
161 earthquakes of the Fars arc are located within the so-called “Competent Group” of mechanically-

162 strong platform carbonates that make up the middle-to-lower sedimentary cover at depths of ~5–  
163 10 km (Nissen et al., 2010, 2011, 2014; Lohman & Barnhart 2010; Roustaei et al., 2010;  
164 Barnhart et al., 2013; Elliott et al., 2015). At the same time, a number of microseismic studies  
165 have indicated concentrations of small earthquakes at probable basement depths of ~10–20 km  
166 (e.g. Tatar et al., 2004; Nissen et al., 2011). Helping to reconcile these differences, a recent  
167 relocation of the 70-year catalog of well-recorded, moderate to large earthquakes indicated a  
168 focal depth range of 4–25 km (Karasözen et al., 2019). Till now, the largest instrumental  
169 earthquakes in the Fars arc have not exceeded  $M_w$  6.7, reflecting that the seismogenic layer is  
170 segmented vertically by the Hormuz salt and other weak evaporitic or shale horizons within the  
171 cover, across which seismic rupture cannot propagate (Nissen et al., 2010). This mechanical  
172 segmentation also manifests itself in coseismic slip planes with characteristically narrow (small  
173 width-to-length ratio) dimensions (Roustaei et al., 2010; Elliott et al., 2015).

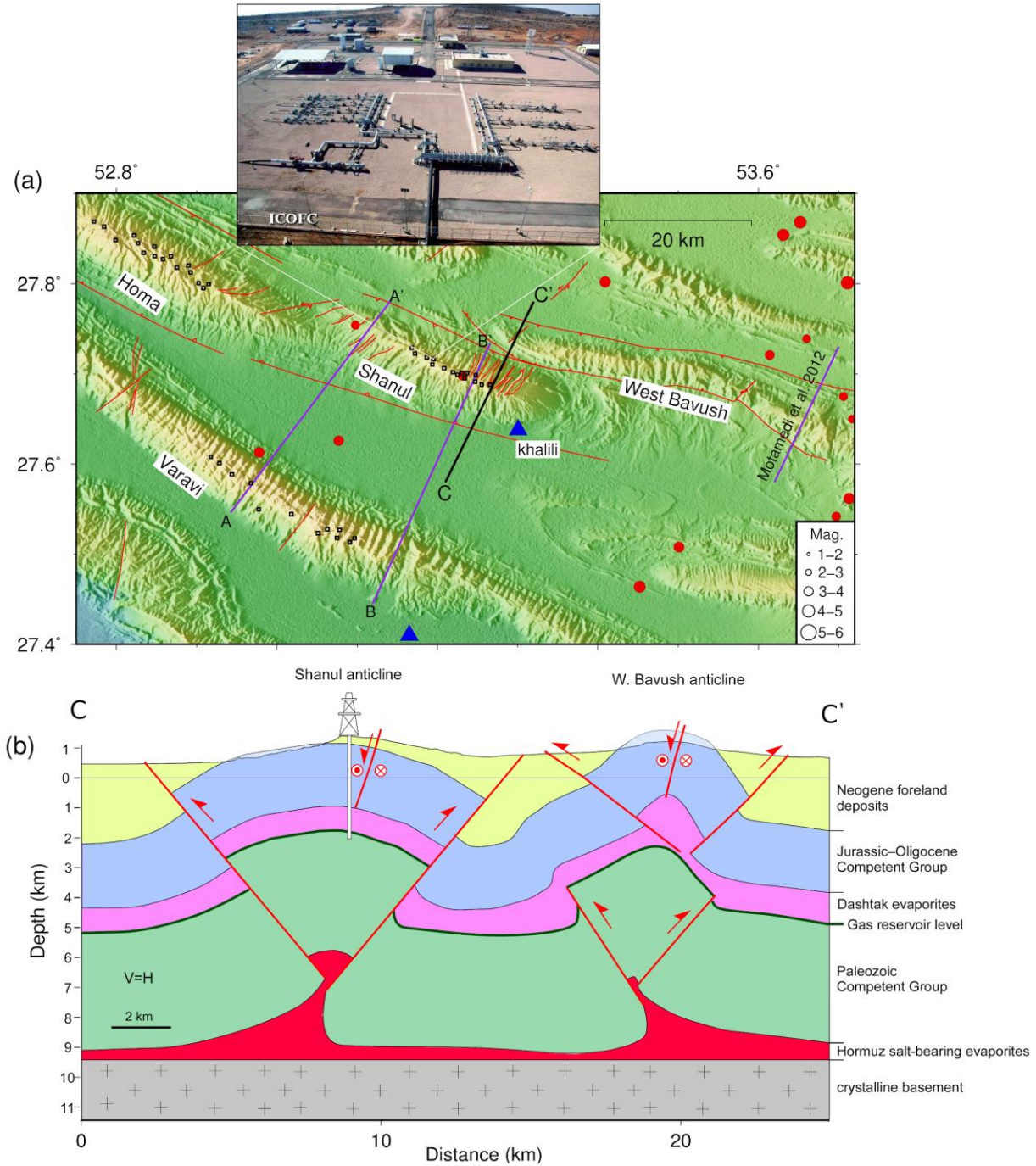
174

## 175 **2.2. Geologic structure, production history, and background seismicity of the study area**

176 The Shanul field is part of a concentration of natural gas reservoirs in the central and western  
177 Fars arc (Figure 1b). This region is characterized by symmetric to weakly-asymmetric  
178 “whaleback” folds with characteristic wavelengths of ~10–20 km and amplitudes of ~2–4 km,  
179 which are controlled primarily by detachment along the Hormuz salt at ~8–12 km depth (Allen et  
180 al., 2013; Motamedi et al., 2012; Najafi et al., 2014). Published seismic reflection imagery shows  
181 that many of the anticlines exhibit “pop-up” geometries accompanied by pairs of opposite-  
182 verging, high-angle reverse faults on both flanks, originating either from the Hormuz detachment  
183 at the base of the cover (Najafi et al., 2014) or a secondary decollement within Triassic Dashtak  
184 evaporites of the middle cover (Figure 2) (Motamedi et al., 2012).

185 The Shanul gas reserves are contained beneath the broad, symmetric Shanul anticline, NW of the  
186 small settlement of Khalili (Figure 2). This anticline is outlined by resistant carbonates of the  
187 Miocene Mishan formation, while its close neighbor to the east — the West Bavush anticline —  
188 is expressed in the Oligocene Asmari limestone (Figure 2). A cross-section of the Shanul  
189 anticline published by the Geological Survey of Iran (GSI) depicts the Shanul anticline as  
190 flanked by steep reverse faults that originate in Paleozoic strata in the anticline core. This view is  
191 supported by our own interpretation of newly-available National Iranian Oil Company (NIOC)  
192 seismic reflection imagery (Figs. S1, S2). In contrast, the West Bavush anticline has a tighter and  
193 more asymmetric (southward divergent) shape, reflecting that its flanking reverse faults originate  
194 at shallower (~3 km) depths in Triassic Dashtak evaporites (Figure 2 and Motamedi et al., 2012).  
195 The faults underlying both anticlines emerge at the surface as longitudinal reverse faults trending  
196 ~N100°–105° (Figure 2). A combination of remote-sensing, field, and seismic data permit us to  
197 construct a structural cross-section across these anticlines, from surface down to the base of  
198 sedimentary cover (Figure 2b).

199



200

201 **Figure 2. a)** Topography, modified map of the faults, background seismicity, the Shanul, and neighboring Homa,  
 202 Varavi, and West Bavush anticlines. The inset photo shows the Shanul gas field, from ICOFC. Black squares show  
 203 the location of active wells in the Shanul, Homa, and Varavi gas fields. Red circles are relocated earthquakes before  
 204 2019 (Karasözen et al., 2019). Blue triangles show IRSC broadband stations. Purple lines show locations of the  
 205 seismic profiles (This study and Motamedi et al., 2012). The A–A' and B–B' seismic sections presented in Figs S1  
 206 and S2. **b)** The structural cross-section across the Shanul and West Bavush anticlines (C–C' profile), constructed  
 207 based on an integration of seismic, field and remote-sensing data.

208 The Shanul reservoir was discovered in 1995 and the first well drilled in 2004, with gas  
209 extraction starting in 2006 from Permo-Triassic Dehram Group carbonates, capped by Dashtak  
210 evaporites at depth of ~3-4 km (Motamedi et al., 2012; Esrafil-Dizaji & Rahimpour-Bonab,  
211 2013). The gas field belongs to the Iranian Central Oil Fields Company (ICOFC), one of the five  
212 major production companies of the NIOC, while the Southern Zagros Oil and Gas Production  
213 Company is responsible for its operation, extraction, and injection. So far, 18 wells have been  
214 drilled in the Shanul gas field (Figure 2). According to the ICOFC, 35 million cubic meters per  
215 day of gas are extracted from the Shanul field and the neighboring Homa reservoir, which  
216 together have a capacity of 220 billion cubic meters. Gas extraction from the 16th well of the  
217 Shanul field commenced in 2016, producing 600,000 cubic meters per day. Considering the gas  
218 capacity and extraction rate, gas reserves from both reservoirs are likely to become depleted  
219 within about 3 years. Fluid injection, which is typically applied in the gas fields of Iran when  
220 production is waning, is therefore likely to have started in both reservoirs.

221 There are no historical records of any earthquake unambiguously linked to faults within our  
222 study area (Ambraseys and Melville, 1982; Berberian, 1995). Modern seismicity in Iran is  
223 monitored and reported by permanent networks of the IRSC and the International Institute of  
224 Earthquake Engineering and Seismology (IIEES), which have been densified with time. Relative  
225 sparse seismic coverage in the Zagros prior to about 2012 limited the routine detection threshold  
226 and location accuracy for small-to-moderate magnitude earthquakes. Nevertheless, the relocated  
227 catalog of Karasözen et al. (2019) indicates two events of  $m_b$  4 (on 10 August 2009 and 1  
228 October 2010) that are collocated with the Shanul anticline (Figure 2).

229

### 230 **3 Source characteristics of the 2019-2020 Khalili seismic sequence**

231

#### 232 **3.1. Multiple-event relocation**

233

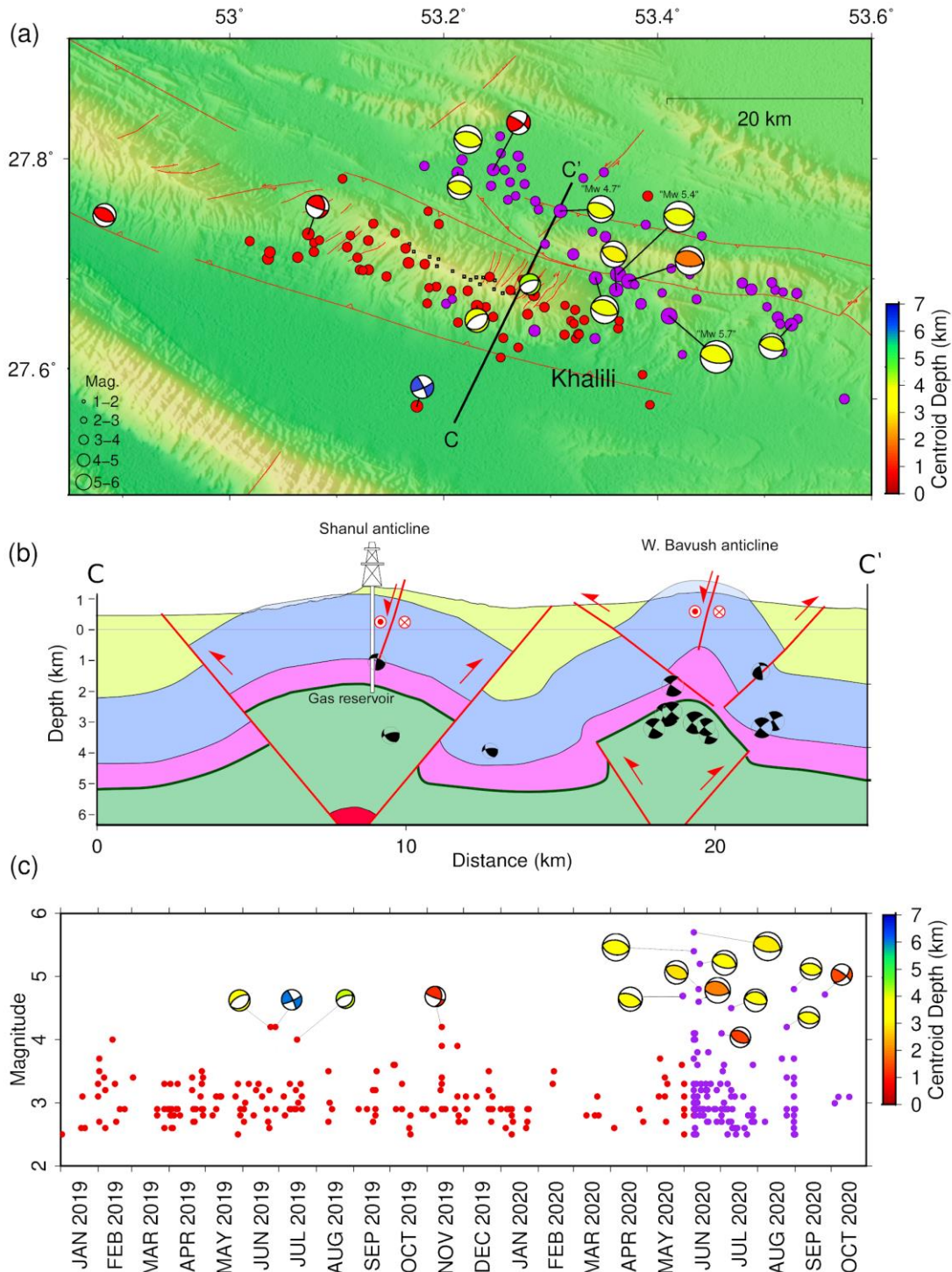
234 Here we assess the overall spatio-temporal evolution of the 2019–2020 sequence using a  
235 multiple-event epicentral relocation. We used the *Mloc* implementation (Bergman & Solomon,  
236 1990) of the hypocentral decomposition algorithm (Jordan and Sverdrup, 1981), consistent with  
237 several earlier regional studies (Nissen et al., 2010, 2019; Roustaei et al., 2010; Elliott et al.,  
238 2015; Karasözen et al., 2019). IRSC station coverage is sufficient (Figure S3) that we could  
239 employ a “direct calibration” (Karasözen et al., 2019) of the 2019-2020 sequence, yielding  
240 epicentral uncertainties of less than ~3 km for most of the selected events (Figure S4). Among  
241 the ~300 events ( $M_n \geq 2.5$ ) reported by IRSC, we relocated 115 events ( $M_n \geq 3.0$ ) with sufficient  
242 numbers of phase readings within epicentral distance of less than 1.8 degree and moderate  
243 azimuthal gaps. We use a slightly modified version of the 1-D layered velocity model (Figure  
244 S5) of Karasözen et al. (2019) to predict theoretical travel times (Figure S6) at local and regional  
245 distances. Owing to insufficient closeby station coverage, we were unable to solve for focal  
246 depths of most events. Among the 115 events, the focal depth of 19 events was constrained with  
247 phase reading from a very nearby station, but for 96 events the focal depths were fixed to 7 km  
248 (Table S3). Therefore the relocated seismicity cannot be used to infer the dip of the causative  
249 faulting at depth. From experience, the errors of the assumed focal depth of less than ~15 km  
250 have a negligible effect on epicenter accuracy (Ghods et al., 2012).

251

252 The spatio-temporal evolution of seismicity clearly depicts two phases of the sequence (Figure  
253 3). Phase 1 started in January 2019 and continued through early 2020, and is swarm-like, lacking

254 a dominant mainshock or clear taper of aftershocks. Phase 1 events follow a WNW–ESE-  
255 oriented trend centered on the southern limb of the Shanul anticline. Phase 2 commenced with  
256 the  $M_w$  4.7 foreshock on May 31, 2020, and includes the June 9, 2020  $M_w$  5.4 and 5.7  
257 earthquakes and their aftershocks. Phase 2 seismicity lies along a separate WNW–ESE-oriented  
258 trend located between the Shanul and West Bavush anticlines (Figure 3).

259



260

261 **Figure 3. (a)** Relocated epicenters of  $M_n \geq 3.0$  events and focal mechanisms of  $M_n \geq 4.0$  events from January 2019

262 to October 2020 that are coloured by centroid depth. Red circles are events in phase 1 (prior to May 31, 2020) and

263 purple circles are those in phase 2. Red lines show modified faults in the region (after the GSI) and black squares

264 show the location of active wells in the Shanul gas field. (b) The structural cross-section across the Shanul and West

265 Bavush anticlines (C–C' profile, and color same as the Figure 2) and our relocated focal mechanisms at their

266 centroid depths. (c) Temporal evolution of seismicity from IRSC catalog ( $M_n \geq 2.5$ ), with events plotted by the

267 magnitude and coloured as in (a).

268 **3.2. Focal depth of the June 9, 2020  $M_w$  5.7 mainshock**

269

270 Well-constrained focal depths are an important potential discriminator of induced earthquakes.

271 We use independent, teleseismic data to estimate the focal depth of the June 9, 2020  $M_w$  5.7

272 Khalili mainshock.

273

274 We modelled the delay between the direct  $P$  arrival and the surface reflected  $pP$  phases at

275 teleseismic distances, which depends on the source depth and the average  $P$  wave velocity above

276 the hypocenter. For this analysis, we used the Array Beam Depth Tool (see *Code Availability*;

277 e.g. Negi et al., 2017). To improve the signal-to-noise ratio, we used array recordings, so that

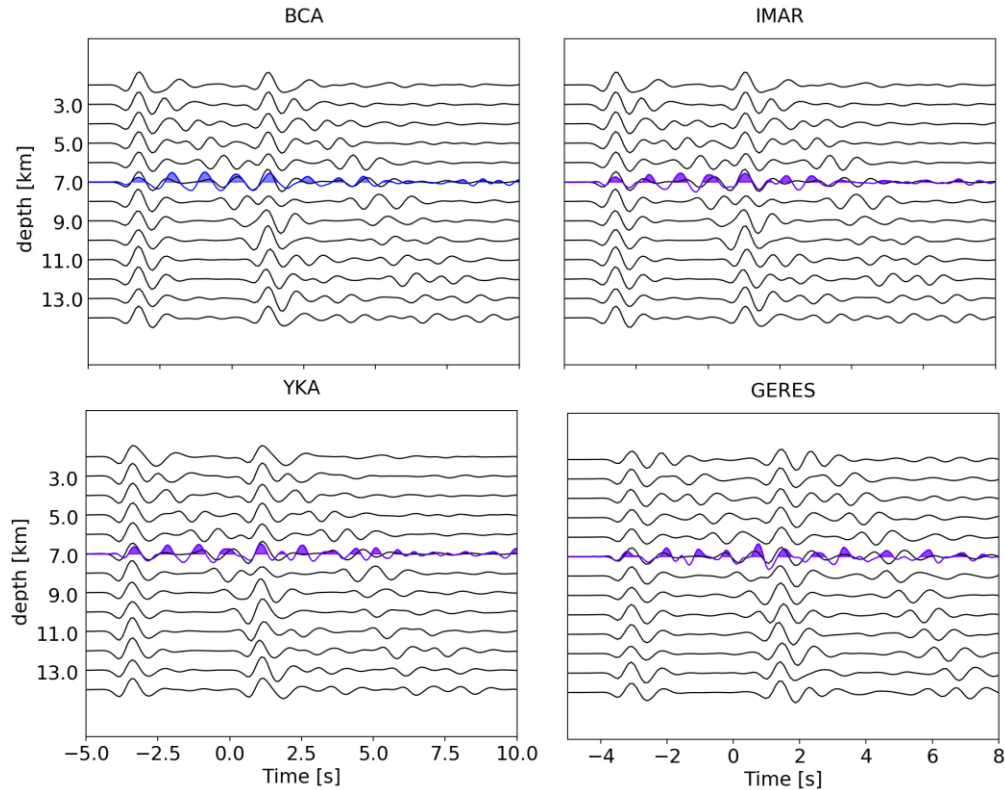
278 similar waveforms can be stacked to form a beam. For this analysis, we processed independently

279 four different seismic arrays (Figure S7). Observed beams are compared to synthetic ones,

280 computed for different source depths using source and receiver crustal models plus a global

281 mantle model. Results from all four arrays are consistent with a focal depth of  $\sim 7$  km for the  $M_w$

282 5.7 earthquake (Figure 4).



283

284

285 **Figure 4.** Estimation of the focal depth of the June 9, 2020  $M_w$  5.7 Khalili mainshock using teleseismic records in  
 286 four seismic arrays; BCA, IMAR, YKA, and GERES (See the location of arrays in Figure S7). Black lines show  
 287 synthetic waveforms including depth phases ( $P$  and  $pP$ ) based on velocity model and source mechanism in different  
 288 depths. Blue waveforms represent observed stacked array beams corresponding to each array. A focal depth of 7 km  
 289 offers the best visual coherency between observed and synthetic traces.

290

### 291 3.3. Regional moment tensor solutions

292

293 Full moment tensor (MT) solutions obtained through regional waveform inversions are a key  
 294 tool for induced seismicity studies, providing critical information on the source geometry and the  
 295 rupture process (e.g. Dahm et al., 2015). Observations of relevant non-double couple (non-DC)  
 296 components through MT decomposition have been used as an indicator for a certain type of  
 297 induced seismicity (e.g. Cesca et al., 2013a; Zhang et al., 2016). For very specific earthquakes,  
 298 e.g. those involving an underground collapse, a full MT inversion can be directly used to detect  
 299 specific induced events (e.g. Cesca et al., 2013a). However, most induced earthquakes are

300 characterized by shear fracturing, and full MT inversions and decomposition results are useful  
301 more for the inference of the rupture geometry than for discrimination. Furthermore, full MT  
302 inversions are challenging for small to moderate magnitude events, requiring a robust assessment  
303 of any resulting non double-couple (DC) source terms. Probabilistic waveform inversion  
304 techniques, which provide estimations of the parameter uncertainties and trade-offs, provide the  
305 best approach to assess reliable non-DC components (Zahradnik et al., 2008; Kühn et al., 2020).  
306 Among the parameters which are estimated by a centroid full MT inversion (scalar moment,  
307 centroid depth, fault plane angles, and percentages of decomposed MT terms), the centroid depth  
308 is particularly important discriminator between anthropogenic and natural seismicity in the  
309 region where both are probable (Dahm et al., 2013; Grigoli et al., 2017).

310  
311 We performed full MT inversions for the four earthquakes in the Khalili sequence; the  $M_w$  5.4  
312 and 5.7 phase 2 events on June 9, 2020 and two events with normal mechanisms in phase 1. We  
313 also undertook deviatoric MT inversion — using the standard decomposition between  
314 compensated linear vector dipole (CLVD) and double couple terms — for eleven moderate  
315 events of  $M_w$  4.0–4.8, including two phase 1 events and seven additional phase 2 events. We  
316 used a probabilistic MT inversion method (Heimann et al., 2018), which provides ensembles of  
317 best-fitting MTs, which are used to estimate uncertainties and trade-offs for all inverted source  
318 parameters. This technique has been successfully applied to other earthquakes in the Zagros, as  
319 well as in other regions (e.g. Kühn et al., 2020).

320  
321 We set up the MT inversion to simultaneously fit 3-components waveforms in the time (full  
322 displacement waveforms) and in the frequency domains (full amplitude spectra). Synthetic  
323 seismograms were computed using pre-calculated Green's functions (Heimann et al., 2019),

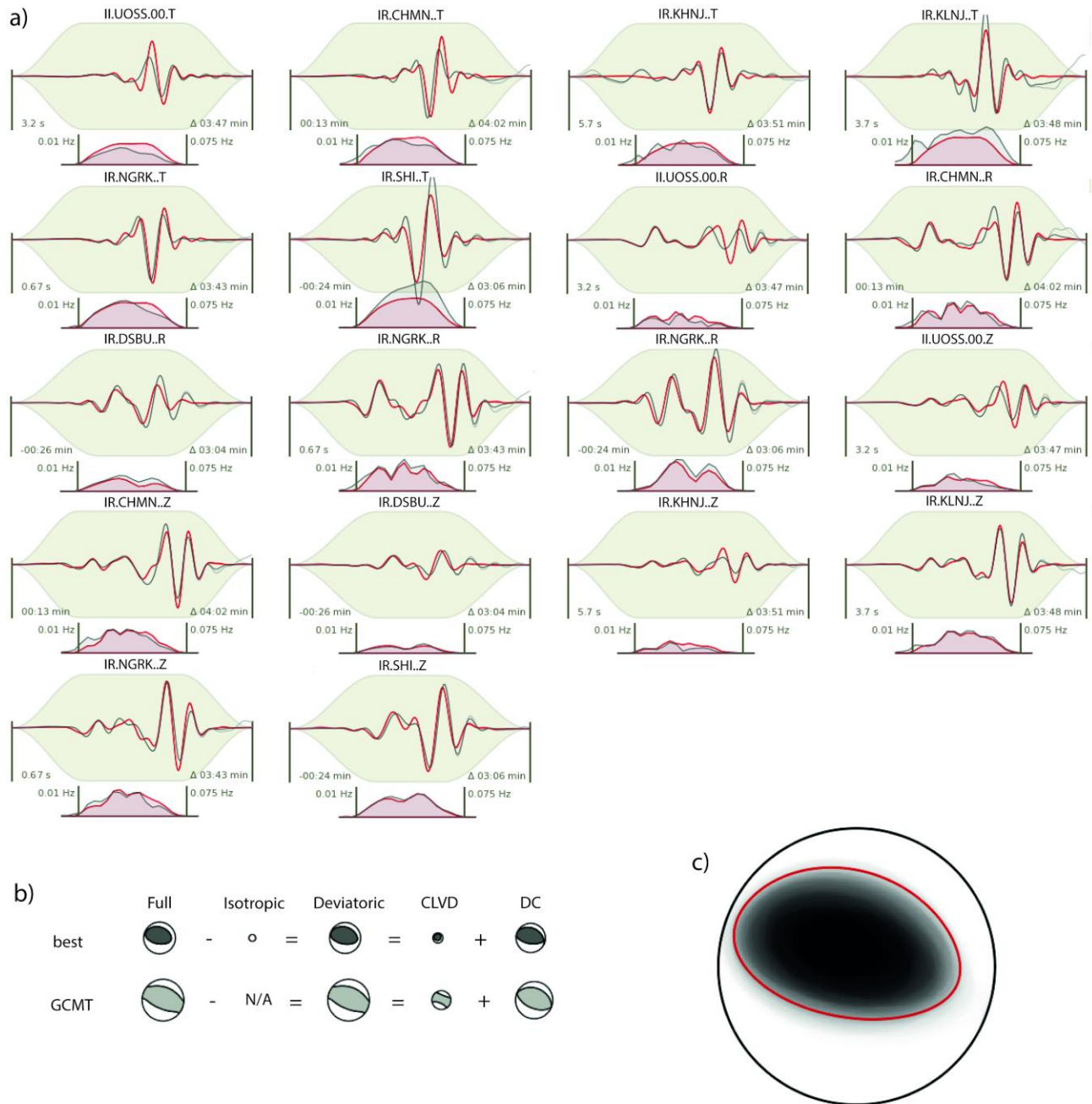
324 based on a velocity model by Karasözen et al., (2019). For events smaller than  $M_w$  5 we adopted  
325 the frequency band of 0.02–0.07 Hz; for the larger pair of events, we used the frequency band  
326 0.015–0.05 Hz. To avoid systematic error in the MT solutions due to sensor misorientation, we  
327 applied the sensor orientation corrections (Braunmiller et al., 2020) for the IRSC stations. The  
328 resolved focal mechanisms are in good agreement with GCMT and GEOFON solutions, for the  
329 few cases when they are available, but we estimate in most cases shallower centroid depths,  
330 mostly  $\leq 4$  km with estimated uncertainties of 0.5 km (note that Global CMT has no resolution  
331 for shallow depths below 15 km). All obtained source parameters together with their  
332 uncertainties (68% confidence intervals) are listed in Table 1.

333  
334 We observe distinct patterns of focal mechanism in the two phases of the 2019-2020 seismic  
335 sequence (Figure 3a). Phase 1 events exhibit diverse mechanisms and depths, comprising one  
336 very shallow (1 km centroid depth) reverse faulting event, two normal faulting events at 3-4 km,  
337 and a slightly deeper (7 km) strike-slip earthquake. The normal faulting events appear linked to a  
338 series of short, shallow, ~NE-trending faults mapped along the crest of the Shanul anticline  
339 (Figs. 2, 3), likely the consequence of bending stresses within the upper layer of the fold. Figure  
340 S8 shows waveform and amplitude spectra fits for the June 24, 2019  $M_w$  4.2 event with normal  
341 mechanism. We observe that for the pair of normal mechanisms, the non-DC part is larger than  
342 the DC part (Figs. S9, S10).

343  
344 Phase 2 seismicity rather follows a typical foreshock-mainshock-aftershock pattern, with similar  
345 ENE–WSW-oriented thrust faulting mechanisms and consistently shallow ( $\leq 4$  km) centroid  
346 depths, suggesting rupture occur along a single fault or fault zone, parallel to both the local fold  
347 axes and the overall seismicity trend. Figure 5 shows waveform and amplitude spectra fits for the

348 June 9, 2020  $M_w$  5.7 mainshock. Our full moment tensor decomposition into isotropic (ISO) and  
349 CLVD and DC components reveals a relatively large CLVD component, similar to that resolved  
350 independently by GCMT and GEOFON. The  $M_w$  5.7 mainshock centroid depth is shallower  
351 ( $3\pm 1$  km) than the focal depth ( $\sim 7$  km, resolved by teleseismic  $pP$ - $P$  delays in Section 3.2),  
352 consistent with upward rupture directivity. In any case, both results point to a shallow source,  
353 within the middle-to-upper sedimentary cover.

354



355  
356

357 **Figure 5.** Full moment tensor solution of the June 9, 2020  $M_w$  5.7 earthquake. **(a)** Waveform fits in time domain and  
358 amplitude spectra for the  $M_w$  5.7 earthquake. Red and gray waveforms/spectra show synthetic and observed records,  
359 respectively. Information on the top of the waveforms fit gives station names with transverse (T), radial (R) or  
360 vertical (Z) components. Numbers within the panels describe the time window and the frequency band **(b)** The  
361 decomposition of the full moment tensor in ISO, CLVD, and DC parts. The symbol size indicates the relative  
362 strength of the components. The Global Centroid Moment Tensor (GCMT) solution is shown for comparison. **(c)**  
363 The fuzzy full MT solution illustrating the uncertainty of the solution.

364

365 **Table 1.** Moment tensor solutions of the 15 events in 2019-2010 Khalili seismic sequence obtained in this study.  
 366 Table columns refer to the event number, date and time in UTC (yyyy-mm-dd hh:mm:ss), relocated latitude and  
 367 longitude, Magnitude ( $M_w$ ), centroid depth, and strikes, dips, and rakes of the two nodal planes with estimated  
 368 uncertainties.

| No | Date and time<br>(UTC) | Latitude <sup>o</sup> | Longitude <sup>o</sup> | $M_w$ | Depth (km) | Strike1 <sup>o</sup> | Dip1 <sup>o</sup> | Rake1 <sup>o</sup> | Strike2 <sup>o</sup> | Dip2 <sup>o</sup> | Rake2 <sup>o</sup> |
|----|------------------------|-----------------------|------------------------|-------|------------|----------------------|-------------------|--------------------|----------------------|-------------------|--------------------|
| 1  | 2019-06-24<br>15:14:08 | 27.677                | 53.231                 | 4.2   | 4.0 ± 1.0  | 244 ± 13             | 62 ± 3            | -85 ± 16           | 53 ± 14              | 28 ± 5            | -99 ± 20           |
| 2  | 2019-06-28<br>09:08:54 | 27.594                | 53.175                 | 4.2   | 6.0 ± 1.0  | 335 ± 24             | 83 ± 2            | 170 ± 46           | 66 ± 2               | 80 ± 2            | 7 ± 2              |
| 3  | 2019-07-16<br>12:02:24 | 27.686                | 53.284                 | 4.0   | 4.0 ± 2.0  | 265 ± 56             | 64 ± 7            | -56 ± 25           | 28 ± 14              | 41 ± 12           | -138 ± 42          |
| 4  | 2019-11-13<br>17:57:45 | 27.737                | 53.073                 | 4.2   | 1.0 ± 0.5  | 6 ± 20               | 37 ± 5            | 163 ± 4            | 110 ± 5              | 80 ± 3            | 53 ± 4             |
| 5  | 2020-05-31<br>23:59:00 | 27.756                | 53.309                 | 4.7   | 3.0 ± 0.5  | 292 ± 5              | 58 ± 4            | 99 ± 5             | 96 ± 5               | 33 ± 3            | 76 ± 8             |
| 6  | 2020-06-09<br>16:08:48 | 27.704                | 53.363                 | 5.4   | 3.0 ± 0.5  | 278 ± 5              | 46 ± 3            | 90 ± 8             | 98 ± 6               | 44 ± 3            | 90 ± 7             |
| 7  | 2020-06-09<br>17:18:12 | 27.669                | 53.411                 | 5.7   | 3.0 ± 1.0  | 97 ± 7               | 58 ± 6            | 79 ± 8             | 297 ± 8              | 33 ± 6            | 107 ± 12           |
| 8  | 2020-06-13<br>22:04:14 | 27.691                | 53.361                 | 4.8   | 3.0 ± 0.5  | 294 ± 4              | 33 ± 2            | 100 ± 6            | 102 ± 4              | 57 ± 1            | 83 ± 4             |
| 9  | 2020-06-13<br>23:15:03 | 27.701                | 53.342                 | 4.6   | 3.0 ± 0.5  | 288 ± 9              | 43 ± 6            | 85 ± 13            | 115 ± 9              | 47 ± 6            | 95 ± 12            |
| 10 | 2020-06-14<br>18:06:00 | 27.698                | 53.373                 | 5.2   | 2.0 ± 0.5  | 296 ± 10             | 35 ± 11           | 110 ± 14           | 92 ± 11              | 57 ± 10           | 77 ± 15            |
| 11 | 2020-07-02<br>00:29:00 | 27.739                | 52.885                 | 4.1   | 1.0 ± 0.5  | 304 ± 6              | 43 ± 10           | 100 ± 9            | 112 ± 8              | 48 ± 11           | 82 ± 8             |
| 12 | 2020-07-10<br>20:14:04 | 27.662                | 53.525                 | 4.5   | 4.0 ± 0.5  | 276 ± 5              | 26 ± 2            | 83 ± 8             | 104 ± 4              | 64 ± 2            | 93 ± 4             |
| 13 | 2020-08-25<br>12:16:00 | 27.788                | 53.213                 | 4.2   | 3.5 ± 0.5  | 280 ± 6              | 48 ± 4            | 90 ± 7             | 100 ± 6              | 41 ± 4            | 90 ± 8             |
| 14 | 2020-08-31<br>03:36:50 | 27.810                | 53.222                 | 4.8   | 3.0 ± 0.5  | 284 ± 3              | 45 ± 2            | 91 ± 2             | 103 ± 3              | 45 ± 2            | 89 ± 3             |
| 15 | 2020-09-08<br>01:34:17 | 27.791                | 53.246                 | 4.3   | 1.5 ± 0.5  | 305 ± 9              | 77 ± 11           | 144 ± 21           | 44 ± 20              | 55 ± 11           | 15 ± 21            |

369

370

371

372

373

374

375

376

377

378

379

380

381 **3.4. Fault geometry and slip distribution of the June 9, 2020  $M_w$  5.7 earthquake from**  
382 **InSAR modeling**

383

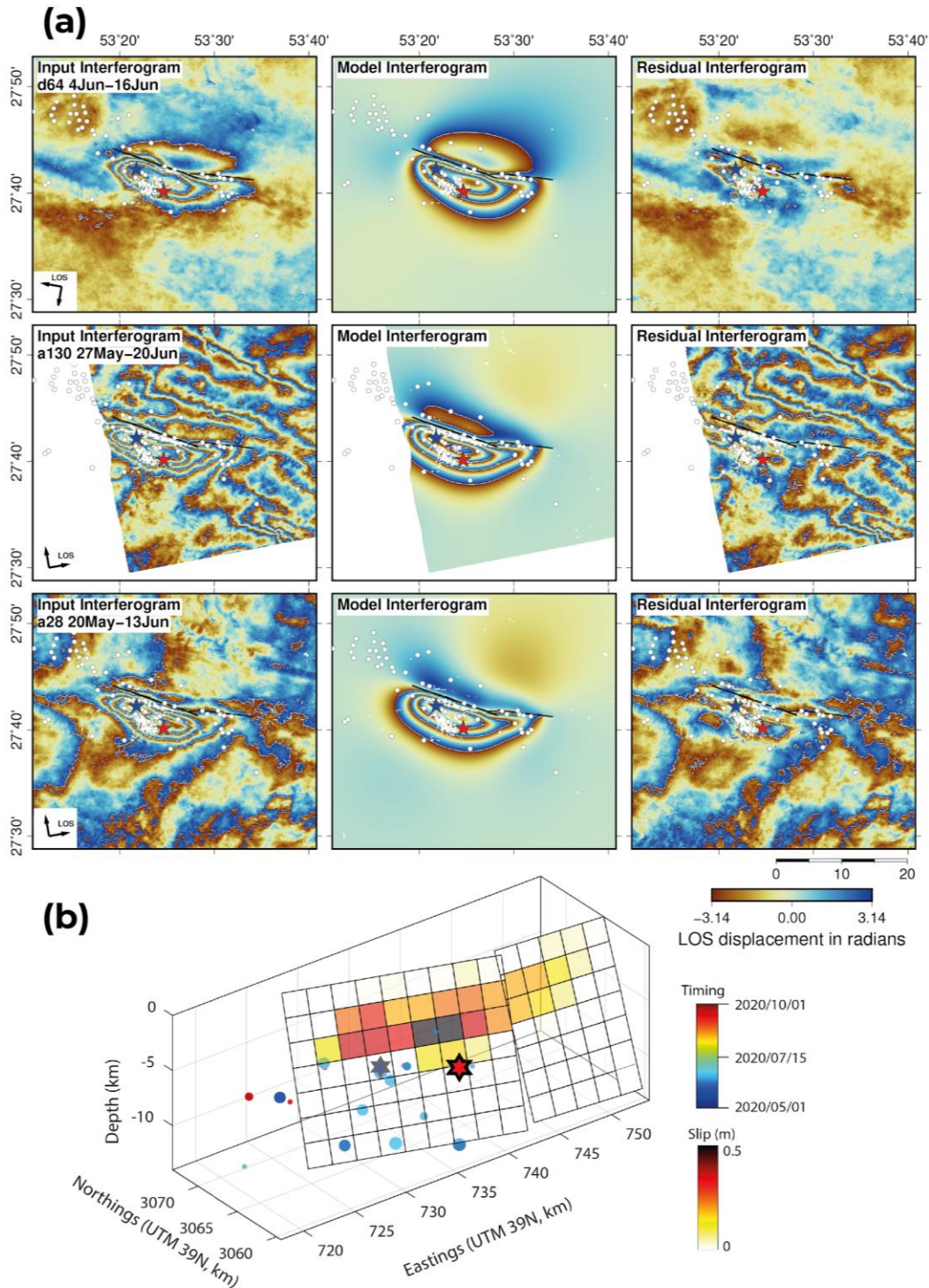
384 We used Sentinel-1 InSAR imagery and elastic dislocation modelling to characterize the June 9,  
385 2020  $M_w$  5.7 mainshock fault geometry and coseismic slip distribution. Using the earliest  
386 available post-seismic acquisitions, we constructed one twelve-day interferogram on descending-  
387 track D64, and two twenty-four-day interferograms on ascending tracks A130 and A28 (Figure  
388 6a). The interferograms also each capture the  $M_w$  5.4 foreshock that occurred 70 minutes before  
389 the mainshock. All three interferograms exhibit a WNW–ESE-oriented pattern of deformation,  
390 containing 3–4 fringes, equivalent to ~10 cm of displacement towards the satellite. The close  
391 similarity of fringe patterns in the descending- and ascending-track interferograms implies that  
392 this deformation is predominantly uplift, centered upon a tight syncline between the Shanul and  
393 West Bavush anticlines. A single fringe (~3 cm) of deformation away from the satellite is also  
394 evident to the North of the main fringe ellipse, collocated with the northern limb of the West  
395 Bavush anticline.

396 To characterize the fault geometry and slip distribution responsible for the observed fringe  
397 patterns, we followed routine elastic dislocation modelling procedures (Okada, 1985; Wright et  
398 al., 1999; Funning et al., 2005) that have been applied to other earthquake sequences in the Fars  
399 arc (e.g. Nissen et al., 2010; Roustaei et al., 2010; Elliott et al., 2015). Full details are provided in  
400 Supplementary text S1. We found that both NNE- and SSW-dipping model faults could  
401 reproduce the overall InSAR deformation pattern, but that in either case, a kinked, two-fault  
402 geometry offered noticeable visual and numerical improvements over a single slip plane. Based  
403 on the adjacency of the mainshock hypocentral locations, as well as the narrow aftershock cloud,

404 our preferred configuration is the SSW-dipping, two-fault model (Figure 6 a,b), though  
405 alternative models are also provided in Supplementary file (Figs. S11–S15).

406 The preferred model faulting parallels the West Bavush anticline but projects to the surface close  
407 to its axial trace, and is thus offset southwards from the SSW-dipping fault interpreted in Figure  
408 3b. The ~15 km-long western InSAR model fault segment strikes  $108^\circ$ , dips  $64^\circ$  N, and has a  
409 rake of  $84^\circ$ ; the shorter ~5 km-long eastern model fault segment strikes  $95^\circ$ , dips  $66^\circ$  N and has a  
410 rake of  $110^\circ$ . Near the mainshock hypocenter, slip is concentrated at depths of ~2–8 km, but  
411 elsewhere it falls within an even narrower range of ~2–6 km (Figure 6b), consistent with the  $3\pm 1$   
412 km centroid depth resolved using seismological data. The hypocenter is located close to the  
413 bottom of the slip patch and at about midway along its length, indicating rupture propagation up-  
414 dip and bilaterally along strike. The upward directivity may be responsible for the extensive  
415 damage in the hanging wall of the mainshock fault, and could help explain the widespread  
416 occurrence of land sliding evident in satellite photographs (Valkaniotis, 2020).

417 The InSAR model moment of  $\sim 6.6 \times 10^{17}$  Nm ( $M_w$  5.8) is roughly 50% larger than that of the  
418 mainshock GCMT and USGS W-phase solutions ( $4.2\text{--}4.3 \times 10^{17}$  Nm,  $M_w$  5.7). The  $M_w$  5.4  
419 foreshock can account for much of the difference, though it is possible that our models also  
420 include a small amount of postseismic afterslip.



421

422 **Figure 6.** (a) From top to bottom: coseismic interferograms on tracks D64, A130, and A28. From left to right:  
 423 observed, model, and residual interferograms. Results are shown rewrapped in order to accentuate deformation  
 424 gradients ( $2\pi$  radians = 2.77 cm displacement). The black line is the surface projection of the model faults. Red and  
 425 blue stars are relocated epicenters of the  $M_w$  5.7 and  $M_w$  5.4 earthquakes, respectively, and white dots are relocated  
 426 aftershocks (phase 2). (b) Coseismic slip distribution from modeling the InSAR data. The model fault is divided into

427 2 km square patches. Red and grey stars are hypocenters of the  $M_w$  5.7 and  $M_w$  5.4 earthquakes, respectively. Circles  
428 show the relocated 20 aftershocks, which the focal depths of them were constrained with phase reading from a very  
429 nearby station, and coloured according to time.

430

#### 431 **4 Discussion: was the 2019–2020 Khalili sequence induced?**

432

433 Observations that unequivocally link a seismic sequence to fluid injection time-series in a gas  
434 field are rare. Here, we have no access to the kinds of production data — such as  
435 extraction/injection time-series, volumes, and pressures of the injected fluid — that could  
436 confirm a causative link to trends in the temporal evolution of seismicity. However, the timing of  
437 the 2019-2020 Khalili sequence is at least consistent with an anthropogenic origin. The first well  
438 in the Shanul gas field was drilled in 2004, and gas extraction started in 2006. However, fluid  
439 injection started later, only after production had peaked. Seismicity in the Shanul gas field  
440 emerged several years after the start of extraction. Time delays of several months or even several  
441 years between the start of production and the emergence of induced seismicity have been  
442 observed in other gas fields. For example, in the Groningen region of the Netherlands the first  
443 earthquake occurred after 28 years of production (Richter et al., 2020), while earthquake  
444 sequences near the Oklahoma Wilzetta and Texas Cogdell oil fields commenced ~20 years after  
445 the initiation of fluid injection (Keranen et al., 2014).

446

447 We can also compare source characteristics of the 2019-2020 Khalili sequence with those of  
448 natural, background seismicity in the Fars arc. Our calibrated relocation of the seismic sequence  
449 reveals two distinct clusters in space and time. The first phase is spatially localized in the  
450 southern part of the Shanul gas reservoir and resembles a swarm without a clear mainshock  
451 (Figure 3c). Three out of four centroid depths (1– 4 km) are close to the probable production

452 levels of the reservoir (~3-4 km), and differ markedly from the ~10-20 km depths typical of  
453 small-to-moderate earthquakes in neighboring parts of the Zagros (e.g. Tatar et al., 2004; Nissen  
454 et al., 2011). This phase also exhibits a wide variety of mechanisms, including two normal  
455 faulting events with significant non-DC components. We interpret that the first phase was  
456 induced by fluid injection in the Shanul gas reservoir. Pore pressure changes can induce or  
457 trigger slip on pre-existing faults (such as those identified in regional geological maps and  
458 seismic lines), and can explain the phase 1.

459  
460 The second phase of the sequence commenced with the  $M_w$  4.7 foreshock on May 31, 2020, and  
461 culminated in the  $M_w$  5.4 and 5.7 earthquakes on June 9. This phase is centered upon the West  
462 Bavush anticline, ~15 km NE of the Shanul reservoir. Similar to the first phase, it is marked by  
463 shallow centroid depths of  $\leq 4$  km. However, unlike the first phase, the second phase exhibits  
464 typical foreshock-mainshock-aftershock patterns and reverse faulting mechanisms that are  
465 compatible with regional tectonic stresses. The June 9, 2020  $M_w$  5.7 mainshock ruptured a steep,  
466 SSW-dipping reverse fault within the core of the west Bavush anticline, nucleating at 7 km depth  
467 but releasing most of its moment at shallower depths of ~2–6 km, within the upper half of the  
468 sedimentary cover. The fault width (~4 km) is thus narrow with respect to the fault length (~20  
469 km), similar to patterns observed elsewhere in the Fars arc and presumably reflecting lithologic  
470 barriers to up- and down-dip rupture propagation (Roustaei et al., 2010; Elliott et al., 2015).

471  
472 Most well-recorded Fars arc earthquakes of similar magnitude to the Khalili mainshock — such  
473 as those at Qeshm Island in 2005–2008, Fin in 2006, and Khaki-Shonbe in 2013 — were  
474 centered in the middle or lower cover (at depths of ~5–9 km), and their aftershock sequences  
475 included concentrations of events at unequivocal basement depths (Nissen et al., 2010, 2014;

476 Lohman & Barnhart 2010; Roustaei et al., 2010; Elliott et al., 2015). The shallow depths of  
477 phase 2 of the Khalili sequence are therefore unusual, but they are not unprecedented. The 2013  
478  $M_w$  6.2 Khaki-Shonbe earthquake ruptured a subsidiary fault plane (southeast of the deeper, main  
479 rupture) at shallow depths of  $\sim 2\text{--}4$  km (Elliott et al., 2015), and the nearby 2014  $M_w$  5.1 Bushkan  
480 earthquake slipped at depths of  $\sim 2\text{--}6$  km (Kintner et al., 2019). We note that both these shallow  
481 slip planes are associated with anticlinal structures containing active gas fields (Khaki-Shonbe  
482 earthquake; the Kangan and Zireh fields and Bushkan earthquake; the Dalan field), though  
483 further study would be needed to assess whether they might also have been induced.

484

485 The depths of phase 2 events are also similar to those reported for induced seismicity associated  
486 with hydrocarbon reservoirs in other regions (e.g. Cesca et al., 2014; Dahm et al., 2015). We  
487 therefore interpret that while the second phase involved the release of background tectonic  
488 stresses, it was likely triggered by stress changes from the first stage or fluid migration, by means  
489 of pore pressure diffusion or poroelastic stresses. Fluid migration may reach large distances of  
490 tens of kilometers (e.g. Goebel et al., 2017), which makes this hypothesis fully compatible with  
491 the location of phase 2 events, and can occur over relatively long time periods. The timing of  
492 such a triggering process cannot be accurately discussed here, due to the lack of knowledge on  
493 local diffusivity conditions and the potential presence of pathways controlling fluid migration,  
494 but a delay of 4-5 months between phase 1 and 2 at  $\sim 10$  km distances appears to be compatible  
495 with previous observations of fluid-driven seismicity (e.g. Hainzl et al., 2012).

496

497 The lack of subsurface fluid flow data and or constraints on geomechanical properties preclude  
498 us from quantifying the likelihood of induced or triggered seismicity through physics-based  
499 probabilistic modeling (Dahm et al., 2015). However, as a check on our interpretation of the

500 2019–2020 Khalili sequence as being of anthropogenic origin, we applied qualitative  
501 discrimination approaches based on a series of questions. Application of the Frohlich et al.  
502 (2016a) criteria support our inference that the Khalili earthquake sequence is induced. Moreover,  
503 we applied a new framework proposed by Verdon et al., (2019), comprising a series of variably  
504 weighted questions with positive numerical scores assigned to characteristics of induced  
505 seismicity (+100%) and negative scores to those of natural events (-100%). Our seismological  
506 analysis allows us to obtain an induced assessment ratio (IAR) of +40% with a high evidence  
507 strength ratio (ESR) of 94.8% (ranging between 0 to 100%) supporting the quality and quantity  
508 of information used in the assessment (Figs. S16, S17). Results strongly support our inference  
509 that the 2019–2020 Khalili seismic sequence was induced.

## 510 **5 Conclusions**

511

512 We present a detailed analysis of the 2019-2020 Khalili seismic sequence in the Fars arc of  
513 Zagros Simply Folded Belt. The proximity of this sequence to the Shanul gas field, from which a  
514 very large volume of gas has been extracted over ~14 years, raised the possibility that these were  
515 induced events. We analysed the sequence using local, regional and teleseismic data, and further  
516 constrained the largest earthquake with InSAR modeling. A comparison with previous  
517 background seismicity highlights the anomalously shallow depths of the 2019–2020 sequence,  
518 suggesting human-induced stress changes related to operation in the Shanul gas field caused the  
519 Khalili seismic sequence. This inference is further supported by the application of a variety of  
520 qualitative indicators, but a more sophisticated, probabilistic assessment would require  
521 injection/extraction data, which are lacking. This is, to our knowledge, the first case of  
522 anthropogenic seismicity directly linked to gas extraction in the Zagros. Triggering of the  $M_w$  5.4

523 and 5.7 events highlights the need to identify large faults in the vicinity of active gas fields, and  
524 to avoid pore-pressure perturbations that could destabilize these faults. Iran already hosts a  
525 significant number of proven hydrocarbon reservoirs and has huge potential for new discoveries.  
526 For instance, in 2019, the NIOC discovered a gas reservoir ~20 km north of the Shanul field,  
527 named Eram, with a very considerable gas capacity. Our results suggest that the exploitation of  
528 these reservoirs should be preceded by risk assessment studies and accompanied by the  
529 implementation of dedicated, sophisticated monitoring, which would allow the seismic activity  
530 to be detected early and its evolution tracked.

531

### 532 **Acknowledgment**

533

534 This work was supported by the International Training Course "Seismology and Seismic Hazard  
535 Assessment" which has been funded by the GeoForschungsZentrum Potsdam (GFZ) and the  
536 German Federal Foreign Office through the German Humanitarian Assistance program, grant  
537 S08-60 321.50 ALL 03/19. Furthermore, M.J. acknowledges support by a grant from the Iran  
538 National Science Foundation (INSF) under a research project number "97013349". E.N. was  
539 supported by the Natural Sciences and Engineering Research Council of Canada through  
540 Discovery Grant 2017-04029, the Canada Foundation for Innovation, the British Columbia  
541 Knowledge Development Fund, and a Tier 2 Canada Research Chair. J.A. L.-C. has also  
542 received funding from the European Union's Horizon 2020 research and innovation program  
543 under the Marie Skłodowska-Curie grant agreement No. 754446 and UGR Research and  
544 Knowledge Transfer Found–Athenea3i; and by project 407141557 of the Deutsche  
545 Forschungsgemeinschaft (DFG, German Research Foundation).

546 Maps were prepared using the Pyrocko toolbox and GMT 5 software. We are grateful to all data  
547 research centers and networks for providing the data used in this study. InSAR interferograms  
548 were made using freely available Copernicus Sentinel data (2017; <https://scihub.copernicus.eu/>).  
549 We are thankful to Gudrun Richter, Christian Heberland, Sebastian Hainzl, Torsten Dahm and  
550 Mir Ali Hassanzadeh for constructive comments on this work.

551 **Data availability**

552

553 The seismic catalog and waveforms of the Iran network were downloaded from the Iranian  
554 Seismological Center available at <http://irsc.ut.ac.ir/>. Regional and teleseismic broadband  
555 seismograms were downloaded from the Incorporated Research Institutions for Seismology  
556 (IRIS) Data Management Center. InSAR interferograms were made using Copernicus Sentinel  
557 data available at <https://scihub.copernicus.eu/>. Information on the Shanul and Homa gas  
558 reservoirs obtained from the Iranian Central Oil Fields Company webpage (ICOFC,  
559 <https://en.icofc.ir/>), Southern Zagros Oil and Gas Production Company  
560 (<https://www.szogpc.com/>), and National Iranian Oil Company (NIOC). The geological map of  
561 the region, which is published by the Geological Survey of Iran (GSI), available at  
562 <https://gsi.ir/en>.

563

564 **Code Availability**

565 Some of the maps were prepared using the Pyrocko toolbox (<https://pyrocko.org/>), and GMT 5  
566 software (<https://www.generic-mapping-tools.org/>). For relocation, we used the mloc program  
567 (<https://seismo.com/mloc/>). The probabilistic source inversion was performed with the Grond  
568 framework (Heimann et al., 2018). InSAR data were processed using GAMMA software  
569 (<https://www.gamma-rs.ch/>) and downsampled and inverted using codes developed by the Centre  
570 for the Observation and Modelling of Earthquakes, Volcanoes and Tectonics (COMET) group  
571 (<https://comet.nerc.ac.uk/>), available from the E.N. upon request. The mainshock focal depth was  
572 calculated using ‘Abedeto’ tools  
573 (<https://github.com/HerrMuellerluedenscheid/ArrayBeamDepthTool>).

574

575

576

577

578

579

580

581

582

583 **References**

584

585 Allen, M. B., Saville, C., Blanc, E. J.-P., Talebian, M., & Nissen, E. (2013). Orogenic plateau growth:  
586 Expansion of the Turkish-Iranian Plateau across the Zagros fold-and-thrust belt. *Tectonics*, 32(2), 171–  
587 190. <https://doi.org/10.1002/tect.20025>

588

589 Ambraseys, N. N., & Melville, C. P. (1982). A history of Persian earthquakes. Cambridge: Cambridge  
590 University Press.

591

592 Barnhart, W. D., & Lohman, R. B. (2012). Regional trends in active diapirism revealed by mountain range-  
593 scale InSAR time series. *Geophysical Research Letters*, 39(8). <https://doi.org/10.1029/2012GL051255>

594

595 Barnhart, W. D., Lohman, R. B., & Mellors, R. J. (2013). Active accommodation of plate convergence in  
596 Southern Iran: Earthquake locations, triggered aseismic slip, and regional strain rates. *Journal of*  
597 *Geophysical Research: Solid Earth*, 118(10), 5699–5711. <https://doi.org/10.1002/jgrb.50380>

598

599

600 Berberian, M. (1995). Master “blind” thrust faults hidden under the Zagros folds: Active basement tectonics  
601 and surface morphotectonics. *Tectonophysics*, 241(3), 193–224. [https://doi.org/10.1016/0040-](https://doi.org/10.1016/0040-1951(94)00185-C)  
602 [1951\(94\)00185-C](https://doi.org/10.1016/0040-1951(94)00185-C)

603

604 Bergman, E. A., & Solomon, S. C. (1990). Earthquake swarms on the Mid-Atlantic Ridge: Products of  
605 magmatism or extensional tectonics? *Journal of Geophysical Research: Solid Earth*, 95(B4), 4943–4965.  
606 <https://doi.org/10.1029/JB095iB04p04943>

607

608 Braunmiller, J., Nabelek, J., & Ghods, A. (2020). Sensor Orientation of Iranian Broadband Seismic Stations  
609 from P-Wave Particle Motion. *Seismological Research Letters*, 91(3), 1660–1671.  
610 <https://doi.org/10.1785/0220200019>

611

612 Cesca, S., Rohr, A., & Dahm, T. (2013a). Discrimination of induced seismicity by full moment tensor  
613 inversion and decomposition. *Journal of Seismology*, 17(1), 147–163. [https://doi.org/10.1007/s10950-](https://doi.org/10.1007/s10950-012-9305-8)  
614 [012-9305-8](https://doi.org/10.1007/s10950-012-9305-8)

615

616 Cesca, S., Grigoli, F., Heimann, S., González, Á., Buforn, E., Maghsoudi, et al. (2014). The 2013 September–  
617 October seismic sequence offshore Spain: A case of seismicity triggered by gas injection? *Geophysical*  
618 *Journal International*, 198(2), 941–953. <https://doi.org/10.1093/gji/ggu172>

619  
620  
621  
622  
623  
624  
625  
626  
627  
628  
629  
630  
631  
632  
633  
634  
635  
636  
637  
638  
639  
640  
641  
642  
643  
644  
645  
646  
647  
648  
649  
650  
651  
652  
653  
654  
655

Dahm, T., Becker, D., Bischoff, M., Cesca, S., Dost, B., Fritschen, R., et al. (2013). Recommendation for the discrimination of human-related and natural seismicity. *Journal of Seismology*, *17*(1), 197–202. <https://doi.org/10.1007/s10950-012-9295-6>

Dahm, T., Cesca, S., Hainzl, S., Braun, T., & Krüger, F. (2015). Discrimination between induced, triggered, and natural earthquakes close to hydrocarbon reservoirs: A probabilistic approach based on the modeling of depletion-induced stress changes and seismological source parameters. *Journal of Geophysical Research: Solid Earth*, *120*(4), 2491–2509. <https://doi.org/10.1002/2014JB011778>

Edey, A., Allen, M. B., & Nilfouroushan, F. (2020). Kinematic Variation Within the Fars Arc, Eastern Zagros, and the Development of Fold-and-Thrust Belt Curvature. *Tectonics*, *39*(8), e2019TC005941. <https://doi.org/10.1029/2019TC005941>

Elliott, J. R., Bergman, E. A., Copley, A. C., Ghods, A. R., Nissen, E. K., Oveisi, B., et al. (2015). The 2013 Mw 6.2 Khaki-Shonbe (Iran) Earthquake: Insights into seismic and aseismic shortening of the Zagros sedimentary cover. *Earth and Space Science*, *2*(11), 435–471. <https://doi.org/10.1002/2015EA000098>

Ellsworth, W. L. (2013). Injection-Induced Earthquakes. *Science*, *341*(6142). <https://doi.org/10.1126/science.1225942>

Esfafili-Dizaji, B., & Rahimpour-Bonab, H. (2013). A Review of Permo-Triassic Reservoir Rocks in the Zagros Area, Sw Iran: Influence of the Qatar-Fars Arch. *Journal of Petroleum Geology*, *36*(3), 257–279. <https://doi.org/10.1111/jpg.12555>

Foulger, G. R., Wilson, M. P., Gluyas, J. G., Julian, B. R., & Davies, R. J. (2018). Global review of human-induced earthquakes. *Earth-Science Reviews*, *178*, 438–514. <https://doi.org/10.1016/j.earscirev.2017.07.008>

Frohlich, C., DeShon, H., Stump, B., Hayward, C., Hornbach, M., & Walter, J. I. (2016). A Historical Review of Induced Earthquakes in Texas. *Seismological Research Letters*, *87*(4), 1022–1038. <https://doi.org/10.1785/0220160016>

Funning, G. J., Parsons, B., Wright, T. J., Jackson, J. A., & Fielding, E. J. (2005). Surface displacements and source parameters of the 2003 Bam (Iran) earthquake from Envisat advanced synthetic aperture radar imagery. *Journal of Geophysical Research: Solid Earth*, *110*(B9). <https://doi.org/10.1029/2004JB003338>

- 656 Ghods, A., Rezapour, M., Bergman, E., Mortezaejad, G., & Talebian, M. (2012). Relocation of the 2006 Mw  
 657 6.1 Silakhour, Iran, Earthquake Sequence: Details of Fault Segmentation on the Main Recent  
 658 Fault. *Bulletin of the Seismological Society of America*, *102*(1), 398–416.  
 659 <https://doi.org/10.1785/0120110009>  
 660
- 661
- 662 Goebel, T. H. W., Weingarten, M., Chen, X., Haffener, J., & Brodsky, E. E. (2017). The 2016 Mw5.1  
 663 Fairview, Oklahoma earthquakes: Evidence for long-range poroelastic triggering at >40 km from fluid  
 664 disposal wells. *Earth and Planetary Science Letters*, *472*, 50–61.  
 665 <https://doi.org/10.1016/j.epsl.2017.05.011>  
 666
- 667 Grigoli, F., Cesca, S., Priolo, E., Rinaldi, A. P., Clinton, J. F., Stabile, T. A., et al. (2017). Current challenges  
 668 in monitoring, discrimination, and management of induced seismicity related to underground industrial  
 669 activities: A European perspective. *Reviews of Geophysics*, *55*(2), 310–340.  
 670 <https://doi.org/10.1002/2016RG000542>  
 671
- 672 Grigoli, F., Cesca, S., Rinaldi, A. P., Manconi, A., López-Comino, J. A., Clinton, J. F., et al. (2018). The  
 673 November 2017 Mw 5.5 Pohang earthquake: A possible case of induced seismicity in South Korea.  
 674 *Science*, *360*(6392), 1003–1006. <https://doi.org/10.1126/science.aat2010>  
 675
- 676 Hainzl, S., Fischer, T., & Dahm, T. (2012). Seismicity-based estimation of the driving fluid pressure in the  
 677 case of swarm activity in Western Bohemia. *Geophysical Journal International*, *191*(1), 271–281.  
 678 <https://doi.org/10.1111/j.1365-246X.2012.05610.x>  
 679
- 680 Heimann, S., Isken, M., Kühn, D., Sudhaus, H., Steinberg, A., Daout, S., et al. (2018). *Grond—A probabilistic*  
 681 *earthquake source inversion framework* (1.0, p. 32813 Bytes, 5 Files). GFZ Data Services.  
 682 <https://doi.org/10.5880/GFZ.2.1.2018.003>  
 683
- 684 Heimann, S., Vasyura-Bathke, H., Sudhaus, H., Isken, M. P., Kriegerowski, M., Steinberg, A., & Dahm, T.  
 685 (2019). A Python framework for efficient use of pre-computed Green’s functions in seismological and  
 686 other physical forward and inverse source problems. *Solid Earth*, *10*(6), 1921–1935.  
 687 <https://doi.org/10.5194/se-10-1921-2019>  
 688
- 689 Jahani, S., Callot, J. P., Letouzey, J., & Frizon de Lamotte, D. (2009). The eastern termination of the Zagros  
 690 Fold-and-Thrust Belt, Iran: Structures, evolution, and relationships between salt plugs, folding, and  
 691 faulting. *Tectonics*, *28*(6). <https://doi.org/10.1029/2008TC002418>

- 692 Jahani, S., Hassanpour, J., Mohammadi-Firouz, S., Letouzey, J., Frizon de Lamotte, D., et al. (2017). Salt  
693 tectonics and tear faulting in the central part of the Zagros Fold-Thrust Belt, Iran. *Marine and Petroleum*  
694 *Geology*, 86, 426–446. <https://doi.org/10.1016/j.marpetgeo.2017.06.003>  
695
- 696 Jordan, T. H., & Sverdrup, K. A. (1981). Teleseismic location techniques and their application to earthquake  
697 clusters in the South-Central Pacific. *Bulletin of the Seismological Society of America*, 71(4), 1105–1130.  
698
- 699 Kangi, A., & Heidari, N. (2008). Reservoir-induced seismicity in Karun III dam (Southwestern Iran). *Journal*  
700 *of Seismology*, 12(4), 519–527. <https://doi.org/10.1007/s10950-008-9104-4>  
701
- 702 Karasözen, E., Nissen, E., Bergman, E. A., & Ghods, A. (2019). Seismotectonics of the Zagros (Iran) From  
703 Orogen-Wide, Calibrated Earthquake Relocations. *Journal of Geophysical Research: Solid Earth*, 124(8),  
704 9109–9129. <https://doi.org/10.1029/2019JB017336>  
705
- 706 Keranen, K. M., & Weingarten, M. (2018). Induced Seismicity. *Annual Review of Earth and Planetary*  
707 *Sciences*, 46(1), 149–174. <https://doi.org/10.1146/annurev-earth-082517-010054>  
708
- 709 Keranen, K. M., Weingarten, M., Abers, G. A., Bekins, B. A., & Ge, S. (2014). Sharp increase in central  
710 Oklahoma seismicity since 2008 induced by massive wastewater injection. *Science*, 345(6195), 448–451.  
711 <https://doi.org/10.1126/science.1255802>  
712
- 713 Kundu, B., Vissa, N. K., Gahalaut, K., Gahalaut, V. K., Panda, D., & Malik, K. (2019). Influence of  
714 anthropogenic groundwater pumping on the 2017 November 12 M7.3 Iran–Iraq border earthquake.  
715 *Geophysical Journal International*, 218(2), 833–839. <https://doi.org/10.1093/gji/ggz195>  
716
- 717 Kintner, J. A., Wauthier, C., & Ammon, C. J. (2019). InSAR and seismic analyses of the 2014–15 earthquake  
718 sequence near Bushkan, Iran: Shallow faulting in the core of an anticline fold. *Geophysical Journal*  
719 *International*, 217(2), 1011–1023. <https://doi.org/10.1093/gji/ggz065>  
720
- 721 Kühn, D., Heimann, S., Isken, M. P., Ruigrok, E., & Dost, B. (2020). Probabilistic Moment Tensor Inversion  
722 for Hydrocarbon-Induced Seismicity in the Groningen Gas Field, The Netherlands, Part 1: Testing.  
723 *Bulletin of the Seismological Society of America*, 110(5), 2095–2111.  
724 <https://doi.org/10.1785/0120200099>  
725
- 726 Lohman, R. B., & Barnhart, W. D. (2010). Evaluation of earthquake triggering during the 2005–2008  
727 earthquake sequence on Qeshm Island, Iran. *Journal of Geophysical Research: Solid Earth*, 115(B12).  
728 <https://doi.org/10.1029/2010JB007710>

729

730 Mansouri-Daneshvar, M. R., Ebrahimi, M., & Nejadsoleymani, H. (2018). Investigation of mining-induced  
731 earthquakes in Iran within a time window of 2006–2013. *Journal of Seismology*, 22(6), 1437–1450.  
732 <https://doi.org/10.1007/s10950-018-9776-3>

733

734 Motamedi, H., Sherkati, S., & Sepehr, M. (2012). Structural style variation and its impact on hydrocarbon traps  
735 in central Fars, southern Zagros folded belt, Iran. *Journal of Structural Geology*, 37, 124–133.  
736 <https://doi.org/10.1016/j.jsg.2012.01.021>

737

738 Najafi, M., Yassaghi, A., Bahroudi, A., Vergés, J., & Sherkati, S. (2014). Impact of the Late Triassic Dashtak  
739 intermediate detachment horizon on anticline geometry in the Central Frontal Fars, SE Zagros fold belt,  
740 Iran. *Marine and Petroleum Geology*, 54, 23–36. <https://doi.org/10.1016/j.marpetgeo.2014.02.010>

741

742 Nissen, E., Yamini-Fard, F., Tatar, M., Gholamzadeh, A., Bergman, E., Elliott, J. R., et al. (2010). The vertical  
743 separation of mainshock rupture and microseismicity at Qeshm island in the Zagros fold-and-thrust belt,  
744 Iran. *Earth and Planetary Science Letters*, 296(3), 181–194. <https://doi.org/10.1016/j.epsl.2010.04.049>

745

746 Nissen, E., Tatar, M., Jackson, J. A., & Allen, M. B. (2011). New views on earthquake faulting in the Zagros  
747 fold-and-thrust belt of Iran. *Geophysical Journal International*, 186(3), 928–944.  
748 <https://doi.org/10.1111/j.1365-246X.2011.05119.x>

749

750 Nissen, E., Ghods, A., Karasözen, A., Elliott, J. R., Barnhart, W. D., Bergman, E. A., et al. (2019). The 12  
751 November 2017 M w 7.3 Ezgeleh-Sarpolzahab (Iran) earthquake and active tectonics of the Lurestan arc.  
752 *Journal of Geophysical Research: Solid Earth*, 124. <https://doi.org/10.1029/2018JB016221>

753

754 Nissen, E., Jackson, J., Jahani, S., & Tatar, M. (2014). Zagros “phantom earthquakes” reassessed—The  
755 interplay of seismicity and deep salt flow in the Simply Folded Belt? *Journal of Geophysical Research:  
756 Solid Earth*, 119(4), 3561–3583. <https://doi.org/10.1002/2013JB010796>

757

758 Negi, S. S., Paul, A., Cesca, S., Kamal, Kriegerowski, M., Mahesh, P., & Gupta, S. (2017). Crustal velocity  
759 structure and earthquake processes of Garhwal-Kumaun Himalaya: Constraints from regional waveform  
760 inversion and array beam modeling. *Tectonophysics*, 712–713, 45–63.  
761 <https://doi.org/10.1016/j.tecto.2017.05.007>

762

763 Okada, Y. (1985). Surface deformation due to shear and tensile faults in a half-space. *Bulletin of the  
764 Seismological Society of America*, 75(4), 1135–1154.

765

- 766 Richter, G., Hainzl, S., Dahm, T., & Zöller, G. (2020). Stress-based, statistical modeling of the induced  
767 seismicity at the Groningen gas field, The Netherlands. *Environmental Earth Sciences*, 79(11), 252.  
768 <https://doi.org/10.1007/s12665-020-08941-4>  
769
- 770 Roustaei, M., Nissen, E., Abbassi, M., Gholamzadeh, A., Ghorashi, M., Tatar, M., et al. (2010). The 2006  
771 March 25 Fin earthquakes (Iran)—Insights into the vertical extents of faulting in the Zagros Simply  
772 Folded Belt. *Geophysical Journal International*, 181(3), 1275–1291. [https://doi.org/10.1111/j.1365-  
773 246X.2010.04601.x](https://doi.org/10.1111/j.1365-246X.2010.04601.x)  
774
- 775 Sherkati, S., Molinaro, M., Frizon de Lamotte, D., & Letouzey, J. (2005). Detachment folding in the Central  
776 and Eastern Zagros fold-belt (Iran): Salt mobility, multiple detachments and late basement control.  
777 *Journal of Structural Geology*, 27(9), 1680–1696. <https://doi.org/10.1016/j.jsg.2005.05.010>  
778
- 779 Talebian, M., & Jackson, J. (2004). A reappraisal of earthquake focal mechanisms and active shortening in the  
780 Zagros mountains of Iran. *Geophysical Journal International*, 156(3), 506–526.  
781 <https://doi.org/10.1111/j.1365-246X.2004.02092.x>  
782
- 783 Tatar, M., Hatzfeld, D., & Ghafory-Ashtiany, M. (2004). Tectonics of the Central Zagros (Iran) deduced from  
784 microearthquake seismicity. *Geophysical Journal International*, 156(2), 255–266.  
785 <https://doi.org/10.1111/j.1365-246X.2003.02145.x>  
786
- 787 Valkaniotis, S., (2020). A large number of #landslides triggered by the June 9 2020 #earthquake in southern  
788 #Iran, mapped using before & after #Sentinel2 images. Landslides, debris falls & avalanches are marked  
789 with yellow-red colors. <https://t.co/SyJt3v3be8> [Tweet]. @SotisValkan.  
790 <https://twitter.com/SotisValkan/status/1274433064572157959>  
791
- 792 Verdon, J. P., Baptie, B. J., & Bommer, J. J. (2019). An Improved Framework for Discriminating Seismicity  
793 Induced by Industrial Activities from Natural Earthquakes An Improved Framework for Discriminating  
794 Seismicity Induced by Industrial Activities from Natural Earthquakes. *Seismological Research Letters*,  
795 90(4), 1592–1611. <https://doi.org/10.1785/0220190030>  
796
- 797 Vergés, J., Saura, E., Casciello, E., Fernández, M., Villaseñor, A., Jiménez-Munt, I., & García-Castellanos, D.  
798 (2011). Crustal-scale cross-sections across the NW Zagros belt: Implications for the Arabian margin  
799 reconstruction. *Geological Magazine*, 148(5–6), 739–761. <https://doi.org/10.1017/S0016756811000331>  
800  
801  
802

- 803 Wright, T. J., Parsons, B. E., Jackson, J. A., Haynes, M., Fielding, E. J., England, P. C., & Clarke, P. J. (1999).  
804 Source parameters of the 1 October 1995 Dinar (Turkey) earthquake from SAR interferometry and  
805 seismic bodywave modelling. *Earth and Planetary Science Letters*, 172(1), 23–37.  
806 [https://doi.org/10.1016/S0012-821X\(99\)00186-7](https://doi.org/10.1016/S0012-821X(99)00186-7)
- 807
- 808 Yeck, W. L., Hayes, G. P., McNamara, D. E., Rubinstein, J. L., Barnhart, W. D., Earle, P. S., & Benz, H. M.  
809 (2017). Oklahoma experiences largest earthquake during ongoing regional wastewater injection hazard  
810 mitigation efforts. *Geophysical Research Letters*, 44(2), 711–717.  
811 <https://doi.org/10.1002/2016GL071685>
- 812
- 813 Zahradnik, J., Jansky, J., & Plicka, V. (2008). Detailed Waveform Inversion for Moment Tensors of M~4  
814 Events: Examples from the Corinth Gulf, Greece. *Bulletin of the Seismological Society of America*, 98(6),  
815 2756–2771. <https://doi.org/10.1785/0120080124>
- 816
- 817 Zhang, H., Eaton, D. W., Li, G., Liu, Y., & Harrington, R. M. (2016). Discriminating induced seismicity from  
818 natural earthquakes using moment tensors and source spectra. *Journal of Geophysical Research: Solid*  
819 *Earth*, 121(2), 972–993. <https://doi.org/10.1002/2015JB012603>